A REVIEW OF RAMAN LIDAR TECHNIQUES FOR ATMOSPHERIC MONITORING AT HOWARD UNIVERSITY BELTSVILLE CAMPUS

Demetrius D. Venable, Ph.D.[1]

Received August 6, 2015, accepted September 11, 2015

Abstract – The Howard University Raman Lidar has been operational since 2004, and provides data in support of research on climate system observations and atmospheric science conducted at the Howard University Beltsville campus. This paper reviews (1) technical aspects of the Lidar system, and (2) data analysis techniques used to recover atmospheric parameters important to meteorological and climate change studies.
Keywords: Lidar, atmospheric measurements

Resumen – La Universidad Howard Raman Lidar ha estado en funcionamiento desde 2004, desde cuando proporciona datos en apoyo de la investigación en las observaciones del sistema climático y la ciencia atmosférica llevados a cabo en el campus de la Universidad de Howard Beltsville. Este artículo expone (1) aspectos técnicos del sistema Lidar, y (2) técnicas de análisis de datos utilizados para recuperar los parámetros atmosféricos importantes para estudios meteorológicos y el cambio climático.
Palabras clave: Lidar, análisis atmosférico

Introduction

The Howard University Beltsville campus is located in Beltsville, Maryland, approximately 20 km north of Washington, DC. The campus consists of 110 acres of undeveloped property located in an area that is undergoing a transition from being primarily rural to light industry and suburban in character. The campus is fully dedicated to research initiatives. Activities at the campus are led by a multidisciplinary group of Howard University faculty and research staff in partnership with federal and state agencies, other academic institutions, and private industries. The current focus at the Beltsville campus is on predictability of weather and climate; weather and air quality monitoring; and hands-on experiences with instrumentation – including operations, maintenance, methodology, measurement capability, data handling, data reduction, and error analysis. The campus offers opportunities for students for experiential learning, research, and mentorship that lead toward advanced degrees in atmospheric sciences, chemistry, physics, engineering, and other disciplines that focus on atmospheric research. Primary funded efforts emphasize providing opportunities for students from underrepresented groups.

[1] Department of Physics and Astronomy, Howard University, Washington, DC 20059. Email: dvenable@howard.edu

Beltsville campus researchers maintain a variety of instrumentation for monitoring atmospheric related parameters and making radiation measurements in support of research activities. A partial listing of selected instrumentation is given in Table 1.

Table 1

Partial listing of instrumentation at the Beltsville Campus

Category	Instrumentation/Measurement Type
Meteorology	Air Temperature, Relative Humidity, Air Pressure, Wind Sensor, Infrared Gas Analyzer, Sonic Anemometer
Soil and Precipitation	Thermocouple, Time Domain Reflectometer, Soil and Heat Flux Plate, Rain Gauge, Disdrometer
Chemistry	O_3, NO_x, SO_2, CO, Aerosol Analyzer, Cloud Condensation Nuclei Counter
Radiation	Pyranometer, Multi-filter Rotating Shadow-band Radiometer, Pyrgeometer, Photosynthetically Active Radiation, Solar/Terrestrial/Total Radiation
Remote Sensing	Microwave Radiometer, Ceilometer, Raman Lidar
Sounding	Ozonesonde, Radiosonde

Method

The Howard University Raman Lidar (HURL) has been operational at the Howard University Beltsville campus since 2004. Specifically, the Lidar program collects data to complement other instruments located at the campus, supports efforts of funding agencies, and investigates atmospheric dynamics with emphasis on water vapor mixing ratio in the troposphere. The Lidar is used to characterize temporal and vertical distributions of water vapor and dynamics processes both within and above the planetary boundary layer. Water vapor is important when considering atmospheric chemistry, radiation, and dynamics. Because of its variability in the atmosphere, water vapor provides challenges to measuring high resolution temporal and spatial profiles over the full range of the lower troposphere, upper troposphere, and lower stratosphere. Water vapor is a critical component for predicting weather and monitoring climate change (Whiteman, Vermeesch, Oman, & Weatherhead, 2011). The Raman Lidar group has engaged in developing enhancements for Lidar measurement techniques, developing technology for independently characterizing Raman Lidar system parameters, and technology transfer of methods and techniques developed in our laboratories to the broader scientific community.

The Raman Lidar is based on Raman scattering by nitrogen and water vapor molecules. The amount of energy lost in the inelastic scattering event is characteristic of the scattering molecule. The energy shifts for the scattered photons when molecules are excited from the ground state to the first excited vibrational state for nitrogen and water vapor are 2330.7 cm^{-1} (Long, 2002), and 3654.0 cm^{-1} (Avila, Fernández, Tojeda, & Montero, 2004), respectively. HURL utilizes the third harmonic of a Nd-YAG laser at a wavelength of 354.7 nm. The corresponding wavelengths of the scattered photons are thus 386.7 nm for nitrogen scattering and 407.5 nm for water vapor scattering.

HURL is a custom designed coaxial Lidar system that makes both daytime and nighttime measurements of atmospheric water vapor and aerosols. The Lidar uses narrow bandpass interference filters and a narrow field-of-view telescope to measure: (1) the Rayleigh-Mie and pure rotational Raman signals at 354.7±0.13 nm; (2) the Raman scattered photons from nitrogen molecules at 386.7±0.13 nm; and (3) the Raman scattered photons from water vapor molecules at 407.5±0.13 nm. These three wavelength regions are referred to as the three channels of the system, *i.e.*, the Rayleigh-Mie channel for elastic and pure rotational scattering in the vicinity of 354.7 nm (the "Rayleigh-Mie" channel); and the two Raman channels – the "nitrogen" channel and the "water vapor" channel (Venable et al., 2005; Adam et al., 2010). The primary outputs from HURL are water vapor mixing ratios and aerosol scattering ratios derived from the backscattered Lidar signals. The next section gives the appropriate equations for these quantities.

Lidar Equations

The Raman Lidar equation gives the number of scattered photons, P, detected at range z and wavelength.

$$P(\lambda_X, z) = P_L(\lambda_L)\frac{ct}{2}O_X(z)\frac{A}{z^2}F_X(T)\xi(\lambda_X)N_X(z)\frac{d\sigma_{total}(\lambda_X,\pi)}{d\Omega}\exp\left[-\int_0^z\left[\alpha(\lambda_L,z')+\alpha(\lambda_X,z')\right]dz'\right]+B(\lambda_X) \quad (1)$$

Here the subscript X refers to the channel (X→L for Rayleigh-Mie, X→N for nitrogen, or X→H for water vapor) being considered, P_L is the initial number of photons transmitted by the laser at wavelength l_L, O is the overlap function, A is the area of the telescope collector, $ct/2$ is the effective spatial pulse length where c is the speed of light and t is the laser pulse duration or the measurement integration time, N is the number density of scattering particles, $ds(l,p)/dW$ is the total scattering cross section, x is the overall system efficiency, a is the atmospheric extinction coefficient, and B is the number of background photons. The quantity $F(T)$ contains the temperature dependence (Whiteman 2003a) of the Lidar equation and is given by:

$$F_X(T)=\frac{\int_{\Delta\lambda_X}\frac{d\sigma_X(\lambda,T,\pi)}{d\Omega}\xi(\lambda)d\lambda}{\frac{d\sigma_X(\pi)}{d\Omega}\xi(\lambda_X)} \tag{2}$$

The overall system efficiency, *x(l)*, can be expressed as the product of the optical efficiency factor, *e(l)*, and all other efficiencies of the system, *k(l)*; the latter of which can be assumed constant over the narrow bandwidths of the interference filters:

$$\xi(\lambda)=\varepsilon(\lambda)\kappa(\lambda) \tag{3}$$

In this paper, we will utilize the relationships:

$$S(\lambda,z)=P(\lambda,z)-B(\lambda,z) \tag{4}$$

and

$$\Delta\tau(\lambda_X,\lambda_Y,z)=\exp\left[-\int_0^z\left[\alpha(\lambda_X,z')-\alpha(\lambda_Y,z')\right]dz'\right] \tag{5}$$

For Rayleigh-Mie scattering (Rayleigh-Mie channel) the applicable Lidar equation is (Whiteman, 2003a)

$$S(\lambda_L,z)=P_L(\lambda_L)O_L(z)\frac{A}{z^2}\frac{ct}{2}\xi(\lambda_L)\left(F_X(T)\beta^{molecule}(\lambda_L,z)+\beta^{aero}(\lambda_L,z)\right)\exp\left[-2\int_0^z\left[\alpha(\lambda_L,z')\right]dz'\right], \tag{6}$$

and

$$\beta^{molecule}=N_X(z)\frac{d\sigma(\lambda_L,\pi)}{d\Omega}. \tag{7}$$

Here b^{aero} is the backscatter coefficient for Mie scattering from aerosols and $b^{molecule}$ is the backscatter coefficient for molecular scattering.

Water Vapor Mixing Ratio: The water vapor mixing ratio, *w*, is defined as the mass of water vapor (in kilogram) per kilogram of dry air. The quantity *w* may be written as (Venable et al., 2011):

$$w(z)=\frac{mass_H}{mass_{dryair}}=\frac{N_H(z)M_H}{N_{dryair}(z)M_{dryair}}\approx 0.7808\frac{M_H}{M_{dryair}}\left(\frac{N_H(z)}{N_N(z)}\right) \tag{8}$$

The quantities $mass_H$ *and* $mass_{dryair}$ are the masses of the water vapor and dry air, respectively and *M* is molecular weight. As above, the subscript H represents water vapor and the subscript N represents nitrogen. Since nitrogen is well-mixed in the lower atmosphere, we assume that dry air is composed of approximately 78.08% nitrogen and substitute $N_N \approx 0.7808\ N_{dryair}$. Using Eq. 8 and substituting for the

molecular weights of water vapor ≈18.02 g/mole and dry air ≈28.97 g/mole, we see that $w(z)$ is derivable from the ratio of measurements of $S(l_H, z)$ and $S(l_N, z)$, *i.e.*,

$$w(z) \approx 0.486 \frac{\kappa(\lambda_N)\frac{d\sigma_N(\pi)}{d\Omega}\varepsilon(\lambda_N)}{\kappa(\lambda_H)\frac{d\sigma_H(\pi)}{d\Omega}\varepsilon(\lambda_H)} \frac{O_N(z)}{O_H(z)} \frac{F_N(T)}{F_H(T)} \frac{S(\lambda_H, z)}{S(\lambda_N, z)} \Delta\tau(\lambda_N, \lambda_H, z) \tag{9}$$

Aerosol Scattering Ratio: The aerosol scattering ratio, A_{SR}, is defined as the ratio of the total scattering coefficient (aerosol plus molecular) to the molecular scattering coefficient,

$$A_{SR} = \frac{\beta_{aerosol} + \beta_{molecular}}{\beta_{molecular}}. \tag{10}$$

Using Eqs. 1, 6, and 10, we see that A_{SR} is derivable from the ratio of measurements of $S(l_L, z)$ and $S(l_N, z)$, *i.e.,* (Whiteman, 2003b):

$$A_{SR}(z) \approx 1 + .7808 \frac{\frac{d\sigma_t(\lambda_N, \pi)}{d\Omega}\varepsilon(\lambda_N)}{\frac{d\sigma_t(\lambda_L, \pi)}{d\Omega}\varepsilon(\lambda_L)} F_N(T) \frac{O_N(z)}{O_L(z)} \frac{S(\lambda_L, z)}{S(\lambda_N, z)} \Delta\tau(\lambda_N, \lambda_L, z) - F_L(T). \tag{11}$$

A_{SR} is typically calibrated (normalized) by setting Eq. 10 equal to 1 in a region of the atmosphere that is expected to be free of aerosols. This condition is usually met at high altitudes when cirrus clouds, volcanic ash, smoke, etc. are known not to be present.

Simplified Lidar Return

A simplified model of the behavior of the Lidar equation reveals that without the overlap term the returned signal would primarily decrease as $1/z^2$ as the range (altitude) increases (Wandinger, 2005). This is indicated by the dashed lines (green – Rayleigh-Mie scattering and blue – Raman scattering) in Figure 1.

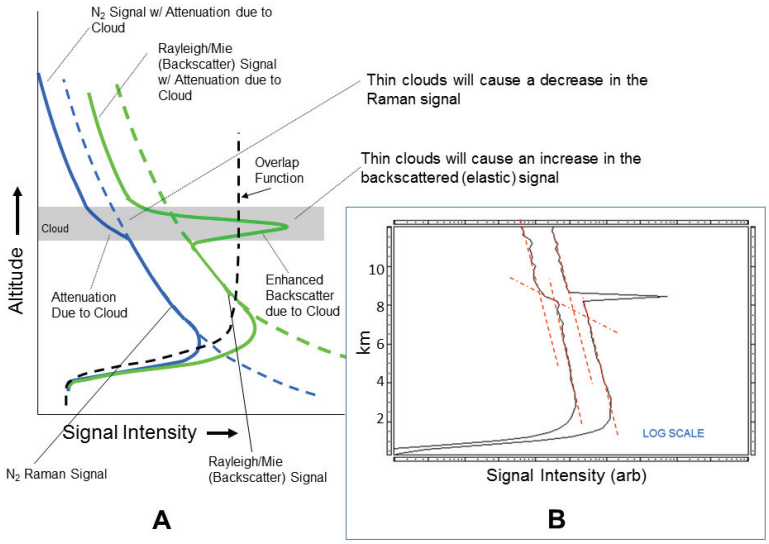

Figure 1. (A) Schematic representation of simplified Lidar returns and (B) actual range corrected Lidar signals plotted on a log scale. For the cases shown in (B) an optically thin cloud was located at an altitude of ~8.5 km. The dashed red lines in (B) are used to highlight changes in the profile shape.

Signals close to the aperture of the telescope (altitude approaches zero) are attenuated due to incomplete overlap of the telescope's field of view and the signal source (Measures, 1984). This region of incomplete overlap is primarily impacted by shadowing of the telescope's secondary mirror and non-optimum focusing of the near field source. Here it is assumed that the telescope is designed for focusing of a source located at infinity. An idealized overlap function ranging from a value of 0 at ground level to a value of 1 at an altitude that corresponds to complete overlap of the source and the telescope's field of view is represented by the dashed black line. Because of the incomplete overlap the actual detected signal starts near 0 in the near field and increases to a local maximum value near the region of complete overlap. The described behavior is the same for both the Rayleigh-Mie and Raman channels. The overlap factor in Eqs. 1 and 6 correct for this behavior. The solid green and blue lines at low altitudes indicate the behavior of the idealized signal at altitudes near zero. In a region of optically thin clouds or aerosol layers the Rayleigh-Mie and Raman signals behave differently. The former shows a spike in the return signal due to the impact of $b^{aerosol}$. The Raman signal shows enhanced attenuation of the return signal. Both show possible attenuation of the laser by the aerosol layer. We assume that the cloud or aerosol layer is optically thin so that the transmitted and return photons are not totally attenuated by the layer. The resulting

signals are depicted by the solid green (Rayleigh-Mie) and solid blue (Raman) lines. Actual signals from the Lidar system are shown in Figure 1B where a thin cloud is located at approximately 8.5 km. These signals show the same basic characteristics as described by the simple model.

HURL system block diagram

A block diagram of the HURL system is shown in Figure 2. The system is capable of operating in either external or internal trigger modes. The former mode is required when other Lidar systems using the same wavelengths are co-located with HURL. The laser is a Continuum Model 9030 operated at 30 Hz with average output power of 10 to 12 W. Prior to transmission into the atmosphere, the beam's diameter is expanded by a factor of 15 to make the laser eye safe to fixed-wing airplanes flying overhead. The beam is transmitted coaxially with the optical axis of the telescope. The receiving telescope has a 16 inch diameter primary mirror and is a fiber optic coupled f/3 system with a field of view of 250 mrad. The system is designed to maintain thermal stability against bore sight misalignment at ±15 C (Venable et al., 2005).

The wavelength separation unit (l Separator in Figure 2) is optically fiber coupled to the focus of the telescope and uses a combination of collimating lenses, narrow bandpass (Dl ≈ 0.25 nm) interference filters, and dichroic beam splitters to extract the desired wavelengths from the collected light signal. The wavelength separation unit directs the light of interest (photons at 354.7, 386.7, and 407.5 nm) to three separate photomultiplier tubes. The photomultiplier signals are analyzed with

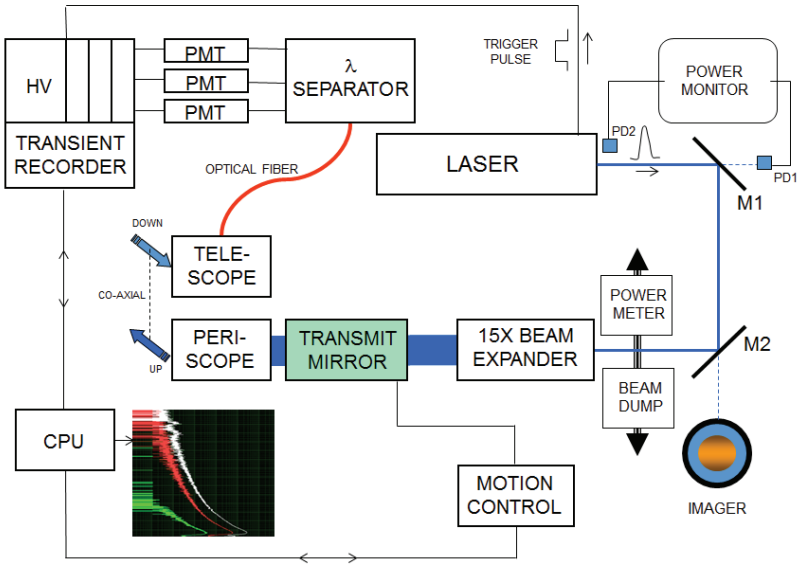

Figure 2. HURL system block diagram.

the use of Licel® transient recorders [Licel GmbH]. These recorders simultaneously utilize analog and photon counting circuitry. The signals are combined by a process referred to as "gluing" (Walker, Venable, & Whiteman, 2014; Adam et al., 2010; Whiteman et al., 2006) that provide an effective dynamic range that is significantly larger than that of either photon counting or analog detection used individually. These recorders accumulate data in 16,000 bins at an integration time of 50 ns per bin resulting in a spatial (range) resolution of 7.5 m. Data acquisition software was provided by the manufacturer (Licel) in LabVIEW® code [National Instruments Corporation]. Custom data analysis routines have been developed in Mathematica® [Wolfram Research] in partnership with National Aeronautics and Space Administration (NASA) collaborators. In the discussion that follows, the term "profile" is used to represent cumulative acquisitions over all 16,000 bins of the transient recorder. These data are typically accumulated for one minute per profile, but the time may be as short as 1 s per profile.

HURL diagnostics and correction terms

Mapping: We have developed independent techniques for diagnostics of many aspects of the HURL system. These methods, referred to as the "Mapping Technique", are described elsewhere (Venable et al., 2011). These techniques involve scanning a constant light source across the aperture of the receiving telescope and analyzing the signals received at the detector for each of the three channels. The techniques are utilized to some degree in many of the diagnostic methods discussed below. Mapping is performed prior to the beginning of a data collection session. The mapping data are analyzed and used as described below.

Spatial Alignment: Prior to beginning a data collection session, the system must be aligned so that the laser beam remains within the field of view of the telescope for all heights in the desired measurement range. We have developed a semi-automated alignment procedure that scans the laser beam across the sky in a step-wise rectangular pattern within the vicinity of the telescope's optical axis (Walker *et al.*, 2012). This is accomplished by driving the transmit mirror shown in Figure 2 with a Newport PMC 100 Motion Controller and high-resolution electrostrictive actuators. This instrument has micrometer step size resolution which allows the transmit angle of the beam to be controlled to a resolution better than 10 mrad. The system is controlled with a LabVIEW® driver that was developed in-house. The return signal is integrated over a selected range (usually 8-10 km) that is near the top of the desired data collection region. Return signals, s, are plotted against the transmit mirror angular positions, (q, f). When the 3-dimensional pattern (q, f, s) is analyzed a maximum will be observed at the location that coincides with the properly aligned system. The motion controller is then commanded to reset the mirror to this optimum position, thus properly aligning the system. HURL has

been found to be an extremely stable system with respect to alignment. The system will typically operate for several days before the alignment will need adjustment

Response Time: Pulse pile-up may occur if photons arrive at the detector at a rate more rapidly than the detector can respond to them. This situation will result in an undercounting of the number of photons. Response time corrections are calculated assuming a non-paralyzable response (Whiteman, 2003a). For this case the measured count rate can be corrected with the following relationship:

$$\eta_o \approx \frac{\eta}{1-\eta\tau}, \quad \eta\tau < 1. \tag{12}$$

Here, η is the measured photon count rate, τ is the system response time, and η_o is the corrected photon count rate. For our system the response time was found to be 5.0 ns using the zero offset technique. In this technique the analog signals are plotted against the photon count rate in a regime where both detectors would provide accurate results. The photon count rate data are corrected using Eq. 12 for a range of values of the response time, τ, and a linear regression (least squares fit) is used to determine the slope and offset (y-intercept) of the best-fit straight line for the data. Values of τ that are too big will tend to overestimate large values of η_o resulting in too small an offset. When τ is too low, large values of η_o will be underestimated and the offset will be too high. When the correct value of τ is used, the offset will be zero. This technique has been compared to the "sigma fit" model (Whiteman *et al.*, 2006), where the root mean square of the residuals of the linear regression is determined and τ that minimizes this value is selected as the correct response time.

Results of these analyses are shown in Figure 3. The data presented here have count rates between 1 MHz (lower toggle rate) and 30 MHz (upper toggle rate). Both methods give similar results, however, the shallow minimum that is observed for the sigma fit technique leads to larger errors in the determination of the correct response time. Identifying the location of this minimum becomes increasingly difficult as the upper toggle rate is reduced.

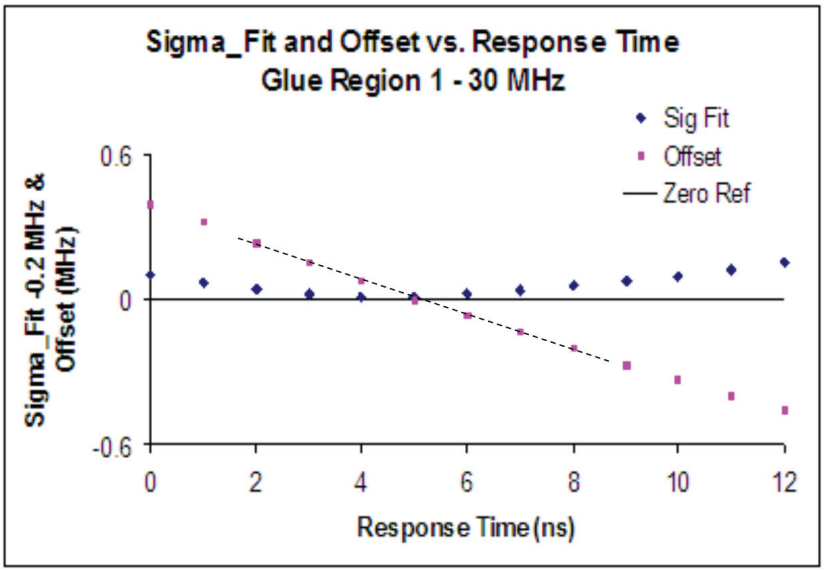

Figure 3. Offset and sigma fit methods for determining the system response time for HURL. A value of 5.0 ns for *t* was found using both the offset and sigma fit methods.

Gluing: Gluing is the process (Walker et al., 2014; Adam et al., 2010; Whiteman et al., 2006) where analog and photon counting data are combined to increase the dynamic range of the detector system. This makes it practical for us to make both near-field and far-field measurements in both daytime and nighttime environments with the single Lidar system. Gluing coefficients, which map the analog signal to a virtual photon count signal, were obtained in a manner similar to that discussed in the subsection "*Response Time*" above. Initially we utilized a procedure whereby coefficients were obtained from individual profiles for a particular data set and average values of all coefficients were then used in a final analysis of the data. This procedure required processing the data twice. Once to obtain the individual profile glue coefficients and a second time to reprocess the data with the average coefficients. Recently we have developed an alternative method for gluing that uses data from the mapping technique (Walker et al., 2014). This method eliminates the need to perform the double processing of the Lidar data. For HURL, the relative differences in the virtual photon count rates obtained when glued with coefficients determined from the mapping technique and virtual photon count rates for the data glued with coefficients determined from the traditional method for both the water vapor and nitrogen channels are less than 1%. The method of determination of the glue coefficients from the mapping data has been incorporated in the standard procedure for processing HURL data.

Overlap Correction: The overlap correction function (Measures, 1984; Wandinger, 2005) may be determined by ray trace modeling of the Lidar system. Because of the nature of the measurements we take, utilizing the ratio of the signals in two channels as opposed to determining w or A_{SR} from single channel measurements, we only need to be concerned with the ratio of the overlap functions for the two channels of interest, not the individual overlap functions for each channel. For HURL, this overlap ratio is very nearly equal to 1 over the useful measurement range of the instrument. We have confirmed this for water vapor mixing ratio calculations by comparison to radiosonde data. In practice, the small overlap correction function obtained by the radiosonde comparison is applied to the data for water vapor mixing ratio calculations. We are currently investigating methods using the mapping technique to validate our overlap functions for individual channels.

Differential Absorption: Differential absorption (Eq. 5) is approximated using aerosol optical thickness (AOT) values available at NASA Goddard Space Flight Center Aerosol Robotic Network (NASA GSFC Aeronet) and the planetary boundary layer height, h_B, determined from the Lidar data. The aerosol attenuation coefficients obtained from the Aeronet data are scaled to the wavelength of interest using the Angstrom coefficient. Nighttime AOT values are extrapolated from daytime Aeronet measurements. We determine a first order approximation to the differential transmission factor by assuming a constant AOT from the ground level to 0.75 h_B, then a linear decrease in AOT to zero from 0.75 h_B to 1.25 h_B, and no aerosols above 1.25 h_B. The molecular component of the extinction coefficient is determined using the standard number density of neutral atmospheric gas particles.

Temperature Dependence – F(T): Determination of temperature dependence of rotational Raman scattering in the Lidar equation is given by Eq. 2. *F(T)* values for the HURL system were first reported by Adam (2009). Adam gives details of the derivations of the appropriate formulas for determining the scattering cross sections for the Rayleigh-Mie and nitrogen channels based on the works of Herzberg (1950) and of Long (2002). Adam also gives details of the calculation for *F(T)* for the water vapor channel based on the work of Avila et al. (2004). The most recent values of *F(T)* for the nitrogen and water vapor channels using current system parameters for HURL are given by Venable et al. (2011). In practice *F(T)* is calculated and stored in tabular form in a look-up table. These data are interpolated to provide the appropriate correction factor as a function of atmospheric temperature.

Calibration: Typically Lidar data are compared to secondary standard instrumentation for the determination of water vapor mixing ratio calibration constants. Calibration of the water vapor mixing ratio involves the determination of a single constant that will multiply the ratio of the Lidar signals at the water vapor channel to the Lidar signals at the nitrogen channel and convert that ratio to water

vapor mixing ratios. The traditional method has been to compare the Lidar signal ratio to the water vapor mixing ratio obtained from a co-located radio sounding. Radiosondes which are launched at the Beltsville location on a regular basis may provide data for calibration. We have, however, developed an independent method for determination of the water vapor mixing ratio calibration constant using the mapping technique (Venable et al., 2011). For the HURL system, values for the water vapor mixing ratio obtained using the mapping technique agree to within one standard deviation of those obtained from comparison with radiosonde data. For the case of A_{SR}, normalization is performed as stated in the subsection "*Aerosol Scattering Ratio*" above.

HURL data analysis scheme

The data analysis scheme is described in this section. Prior to collection of Lidar data, mapping data and dark current measurements are obtained. A standard start-up procedure that includes system warm-up, laser power optimization, power check, and spatial alignment of the laser beam is followed before data acquisition begins. Immediately before we begin collection of Lidar data, dark current signals are obtained by taking data with the shutters to the photomultiplier tubes closed to prevent light from entering the detectors. These data are used to correct any non-linear biases in the analog signal voltages. Next, data collection begins and individual profiles are accumulated for a specified amount of time, typically one minute. After each profile is accumulated, both analog and photon counting signals are downloaded for all channels and accumulation of a new profile begins.

Preliminary data analysis begins immediately and continues in real-time while Lidar data are being accumulated. The first step in the data analysis is to use the dark current signals to correct the raw data in each bin of the analog signals. Next the photon counting data are corrected for system response time. Ambient background signals are then subtracted from each analog and photon counting data bin. These background signals are obtained from the average signal in the last several thousand bins in each profile. The spatial ranges corresponding to these bins are altitudes beyond the top of the atmosphere (greater than 100 km) and any signals in these bins are thus attributed to background noise. This background is assumed constant over the accumulation time of an individual profile. The analog and photon counting signals are then glued using the gluing coefficients obtained from the mapping experiment. Data are then corrected for incomplete overlap, temperature dependence – $F(T)$, and differential transmission.

Calibration and normalization factors are applied as appropriate. Various data smoothing and averaging routines may be applied to improve signal to noise ratios under some atmospheric conditions. The final products are time-series of profiles for water vapor mixing ratios, aerosols scattering ratios, and their appropriate errors

in both graphical and numerical formats. Typically for graphical representation of the data, the signal intensities in each profile are mapped into a color scale and presented as a color-mapped image that gives the time the profile was obtained on the x axis, height above the ground level on the y axis, and the signal intensity as color variations in the image. See, for example, the color-mapped altitude *vs* time series images of Figures 4 to 6. Numerical data are available in a variety of formats, including ASCII format for the convenience of a broad range of users.

Sample outputs

In this section we present several color-mapped altitude *vs* time series images of HURL data as examples of the final graphical output product. Figure 4 shows data obtained for water vapor mixing ratio measurements when continuously operating the Lidar system for approximately four days. The data collection started at approximately 10:00 UTC on the first day. Local standard time is UTC - 5. The missing data (vertical black lines) correspond to times when the data collection was stopped to clean dew from the Lidar exit window on the roof of the building. At night, the system provides data at much higher altitudes than in the daytime. Low signal to noise ratios in the daytime, primarily due to solar background radiation, reduce the effective range for making measurements.

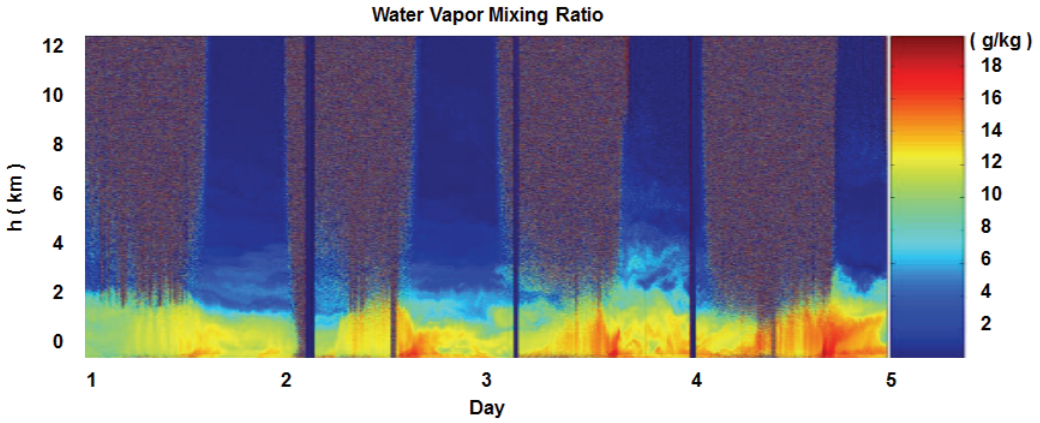

Figure 4. Four days continuous operation of HURL for water vapor mixing ratio.

Figure 5 shows a similar graphical representation for aerosol scattering ratio measurements. Note that A_{SR} data can be obtained at a higher altitude than water vapor mixing ratio data since the Rayleigh-Mie scattering signal is several orders of magnitude larger than the Raman signal. Also note that daytime measurements for A_{SR} can be made at much higher altitudes as compared to the case for w. This is primarily due to the reduced solar background radiation for Rayleigh-Mie scattering near 354.7 nm as compared to the significantly higher solar background radiation

present at the 408.5 Raman scattering wavelength for water vapor molecules. The signal to noise ratio is observed to be reduced above regions with clouds and/or heavy aerosol loading.

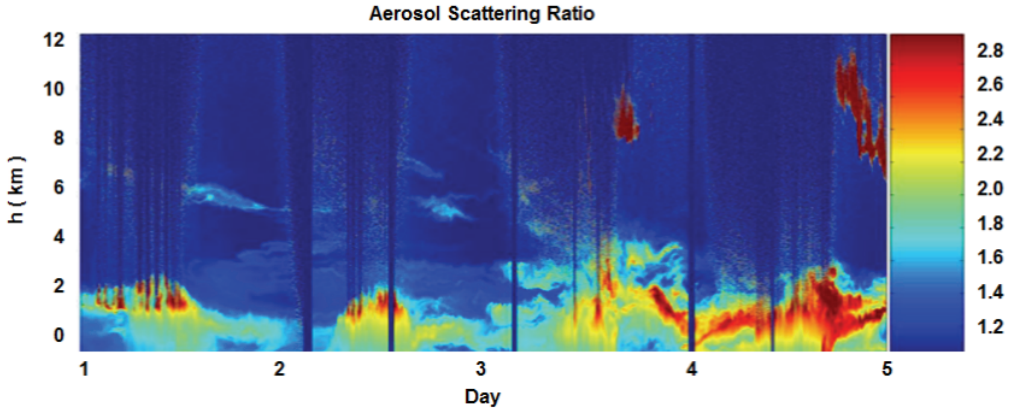

Figure 5. Four days continuous operation of HURL for aerosol scattering ratio. These data were taken at the same time as the data in Figure 4.

As a final example, Figure 6 shows a water vapor mixing ratio color-mapped altitude *vs* time series image for the case were a thin dry layer is observed. The dry layer occurs at an altitude of approximately 0.75 km from 02:40 UTC to 03:50 UTC. The Lidar image captures the development of this layer as well as its dissipation. The abilities of the Lidar to measure the dynamics of features such as these offer significant advantages to modeling efforts. The data in this image are shown at 7.5 m spatial resolution and 1 minute temporal integration. No smoothing has been applied. The ability of the Lidar to measure the dynamics of features such as these is of significant advantage to modeling efforts. Other instruments are not capable of making such measurements at the precision and frequency of the Lidar.

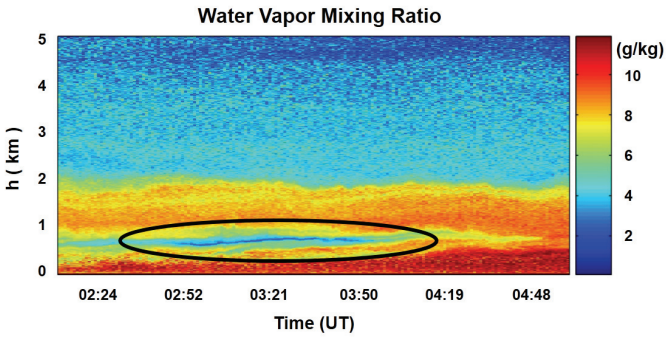

Figure 6. Water vapor mixing ratio showing the development and dissipation of a well-defined dry layer at approximately 0.75 km (black oval). The spatial resolution is 7.5 m.

Summary

Lidar offers many advantages over traditional radiosonde measurements made with weather balloon soundings. The Howard University Raman Lidar has operated episodically for the past 11 years and has made significant contributions to major campaigns carried out at the Beltsville campus. This paper has presented a review of both technical aspects of the Lidar and data analysis techniques for recovery of atmospheric parameters used in meteorological and climate change studies.

We have developed new techniques for Lidar measurements and have led technology transfer efforts to move these to the broader scientific community (Walker, 2013). The HURL system will continue to undergo technological enhancements and upgrades in the future. HURL will continue to play a critical role in the Beltsville campus initiatives for climate system observations and meteorological predictability for the foreseeable future. Finally, much of the technology we have developed will be utilized as atmospheric science researchers at Howard University expand Lidar measurement capabilities to the downtown campus in Washington, DC.

Acknowledgements

The work described in this paper was supported in part by NASA Awards # NNX10AQ11A and # NNX11AJ99G and NOAA Award # NA11SEC4810003. The author would like to acknowledge the numerous contributions of D. N. Whiteman of NASA GSFC to the Beltsville campus Lidar efforts.

Cited literature

Adam, M., Demoz, B. B., Venable, D. D., Joseph, E., Connell, R., Whiteman, A., . . . Fitzgibbon, J. (2010). Water vapor measurements by Howard University Raman Lidar during the WAVES 2006 campaign. *Journal of Atmospheric and Oceanic Technology 27,* 42-60. doi:10.1175/2009JTECHA1331.1

Adam, M. (2009). Notes on temperature-dependent lidar equations. *Journal of Atmospheric and Oceanic Technology*, *26*(6), 1021-1039. doi:10.1175/2008JTECHA1206.1.

Avila, G., Fernández, J. M., Tojeda, G., & Montero, S. (2004). The Raman spectra and cross-sections of H2O, D2O, and HDO in the OH/OD stretching regions. *Journal of Molecular Spectroscopy, 228*(1), 38-65. doi:10.1016/j.jms.2004.06.012.

Herzberg, G. (1950). Molecular spectra and molecular structure. I. Spectra of diatomic molecules. New York: D. van Nostrand Reinhold Inc.

Long, D. A. (2002). The Raman Effect: A unified treatment of the theory of Raman scattering by molecules. New York: John Wiley & Sons. Retrieved from http://www.kinetics.nsc.ru/chichinin/books/spectroscopy/Derek02.pdf.